Achieving ultra-high power factor in Sb_2Te_2Se via valence band convergence

Mohammad Rafiee Diznab[†],[1] Iraj Maleki Shahrivar[†],[1] S. Mehdi Vaez Allae,[1] Yi Xia,[2] and S. Shahab Naghavi[3,*]

[1] *Department of Physics, University of Tehran, Tehran 14395-547, Iran*[†]
[2] *Department of Materials Science and Engineering, Northwestern University, Evanston, Illinois 60208, USA*
[3] *Department of Physical and Computational Chemistry, Shahid Beheshti University, G.C., Evin, 1983963113 Tehran, Iran*

An efficient approach to improve the thermoelectric performance of materials is to converge their electronic bands, which is known as band engineering. In this regard, lots of effort have been made to further improve the thermoelectric efficiency of bulk and exfoliated monolayers of Bi_2Te_3 and Sb_2Te_3. However, ultra-high band degeneracy and thus significant improvement of power factor have not been yet realized in these materials. Using first-principles methods, we demonstrate that the valley degeneracy of Bi_2Te_3 and Sb_2Te_3 can be largely improved upon substitution of the middle layer Te atoms with the more electronegative S or Se atoms. Our detailed analysis reveals that in this family of materials two out of four possible valence band valleys merely depend on the electronegativity of the middle layer chalcogen atoms, which makes the independent modulation of the valleys' position feasible. As such, band alignment of Bi_2Te_3 and Sb_2Te_3 largely improves upon substitution of the middle layer Te atoms with more electronegative, yet chemically similar, S and Se ones. A superior valence band alignment is attained in Sb_2Te_2Se monolayers where the three out of four possible valleys are well-aligned, resulting in a giant band degeneracy of 18 that holds the record among all thermoelectric materials.

Introduction

The electro-thermal energy conversion is an environmentally friendly solution to the global energy crisis, yet the efficiency of energy conversion should be significantly improved for practical applications of thermoelectric (TE) devices [1]. The efficiency of TE materials is determined by the thermoelectric figure of merit $zT = S^2\sigma/(\kappa_e + \kappa_L)$, where σ is the electrical conductivity, S is the Seebeck coefficient or thermopower, T is the absolute temperature, κ_e and κ_L are electronic and lattice contributions to the thermal conductivity, respectively. Achieving an optimal zT value is highly nontrivial, which requires dealing with conflicting parameters, since S and σ are inversely related, and κ_e is proportional to σ as implied by the Wiedemann-Franz law ($\kappa_e = L\sigma T$).

To improve TE performance, various strategies have been proposed, which can be majorly categorized into either i) Phonon engineering [2–5] or ii) Band engineering [6–13]. Thanks to the relatively decoupled nature of lattice thermal transport from the electronic properties, phonon engineering has been frequently utilized to suppress κ_L through creating nanostructures, resulting in a direct boost in zT. On the other hand, band engineering can be typically realized via converging separate energy pockets near the Fermi level (valley degeneracy), thus enhancing the power factor (PF), which is defined as $PF = S^2\sigma$. It should be noted that, increasing S only, for example, through increasing the electron effective mass (m^*), may not ultimately lead to PF enhancement, because it is also detrimental to σ. Therefore, a better scenario is a combination of multiple conducting channels composed of degenerate valleys where every single valley provides a low m^*_{band} and thus high electron mobility [10, 14]. Since the overall density-of-states effective mass is proportional to the orbital degeneracy, $m^*{=}N_v^{2/3}m_b^*$, increasing the number of degenerate valleys simultaneously enhances the Seebeck coefficient, another advantage to attain high PF.

Accordingly, TE materials with intrinsically high N_v and low m_b^* have long been under intensive study, such as PbTe, Bi_2Te_3, Sb_2Te_3, Zintl to name a few. Particularly, Bismuth Telluride and its alloys have attracted considerable amount of attention [14–17] as a practical realization of TE devices. Their excellent TE performance stems from (i) the six-fold degeneracy of the valence-band maximum in the bulk Bi_2Te_3 [18] and (ii) the intrinsically low lattice thermal conductivity of about $\approx$1.5 $Wm^{-1}K^{-1}$[19], resulting in an excellent zT $\approx$1 at T$\approx 320\,K$ [20]. In addition, it has been demonstrated by Dresselhaus *et. al.* [5] that the emergence of quantum confinement effect by reducing the dimensionality could further improve zT. This strategy has been successfully applied to Bi_2Te_3 nanowires, where a 13% enhancement in zT has been achieved compared to the n-type $Bi_2Te_{2.7}Se_{0.3}$ bulk counterpart [21]. Theoretically, exfoliated monolayers of Bi_2Te_3 has been predicted to attain an ultrahigh zT of $\approx$2.7 at $700\,K$ [22].

The present work aims to improve TE efficiency of Bi_2Te_3 and Sb_2Te_3 monolayers, and to suggest design strategies for high-performance TE materials. We show that substitution of the middle layer Te atoms with S and Se improves the valence band alignment in both Bi_2Te_2S and Bi_2Te_2Se monolayers. Particularly we attain an outstanding valence band alignment with N_v of 18 in Sb_2Te_3Se monolayers, which is one of the highest reported N_v values to the best of our knowledge. Meanwhile, all the

* s˙naghavi@sbu.ac.ir
† Contributed equally to this work

studied materials largely benefit from their intrinsically low κ_L due to the strong anharmonicity and heavy average atomic masses [23–26]. Both of these two factors lead to a significant improvement in zT. Therefore, we suggest that solid solutions of $Sb_2Te_{3-x}Se_x$, $Bi_2Te_{3-x}S_x$ and $Bi_2Te_{3-x}Se_x$ with x=1, are more advantageous than their parent compounds for TE applications. It is also worth noting that all the studied compounds in the present work are thermodynamically stable in their bulk phase [27–29] and have been predicted to be exfoliable with dynamically stable monolayers [30]. The bulk Sb_2Te_2Se, Bi_2Te_2S and Bi_2Te_2Se have been experimentally synthesized [31].

Computational Methods

In this study, we performed theoretical calculations using the Density Functional Theory (DFT) as implemented in the Vienna ab-initio Simulation Package (`VASP`) [32, 33]. The projector augmented wave (PAW) pseudopotentials [34, 35], plane wave basis set, and Perdew-Burke-Ernzerhof (PBE) exchange-correlation functionals were used [36] throughout the calculations. The cut-off energy was set to 500 eV and a $24 \times 24 \times 1$ k-mesh sampling was used to ensure tight energy convergence. All structures were fully relaxed with respect to lattices and positions until the forces on each atom become less than 0.1 meV·Å^{-1}. Due to the importance of Spin Orbit Coupling (SOC), we also considered this correction when calculating the electronic structure. Electronic transport properties, namely κ_e, σ and S, were calculated by solving the Boltzmann Transport Equation (BTE) within the constant relaxation time approximation as implemented in `BoltzTraP` [37]. Therein, the Brillouin zone (BZ) was sampled using a dense k-grid of 48×48×1 to ensure accurate interpolation of the Kohn-Sham eigenvalues for `BoltzTraP`. To obtain the second order Inter-atomic Force Constants (IFCs), we used the finite displacement method as implemented in `Phonopy` [38] code using a $4 \times 4 \times 1$ supercell with a k-mesh of $3 \times 3 \times 1$. Third order IFCs were calculated by the `ShengBTE` code [39] using $3 \times 3 \times 1$ supercells, with the corresponding interaction cut-off being set to the third nearest neighboring shell and $4 \times 4 \times 1$ k-mesh sampling of the Brillouin zone.

Results and Discussion

Crystal Structure. Sb_2Te_3 and Bi_2Te_3 have the space group $R\bar{3}m$ with a rhombohedral crystal structure that belongs to the hexagonal crystal family. The bulk structure consists of quintuple layers, held together by the weak van der Waals (vdW) interaction [40, 41]. According to existing experiments [30, 42], monolayers of Bi_2Te_3 and Sb_2Te_3 can be exfoliated from their bulk phase at an energetic cost of 25 meV/Å^2, which is comparable to the cost of peeling off a single layer of graphene from graphite. Therefore both compounds can be categorized as experimentally exfoliable materials [30].

A closer look over the crystal structure of Bi_2Te_3 (likewise Sb_2Te_3) reveals that there are two unique kinds of Te atoms in each monolayer, and thus can be labeled as $Bi_2[Te_{(1)}]_2[Te_{(2)}]$. In the Bi_2Te_3 monolayers, the number of valance electrons responsible for bonding reaches twenty-four per unit-cell, with four from each of the outer layer Te atoms (referred to as $Te_{(1)}$ hereafter), five from each of the Bi atoms and six from the middle layer Te atoms ($Te_{(2)}$). Whereas Bi-$Te_{(1)}$ bond is fairly ionic in its nature, Bi-$Te_{(2)}$ bond is more covalent and weaker [43]. It is thus expected that when one substitutes Te with a more electronegative Se or S atoms, the more weakly bound $Te_{(2)}$ site is energetically preferred, as shown in Fig.1. To get a deeper insight into the electronic structure of the studied monolayers, we use the electron localization function (ELF)[44], which is known to be a potent tool to identify the localization of electrons and the relative orientation of lone electron pairs. The calculated ELF in Figure 1(d) reveals the mushroom shape around the outer layer $Te_{(1)}$ atoms, which evidence the presence of a stereochemically active anionic lone pair with its relative orientation. Our finding is consistent with the previous studies on Bi_2Te_3 [45–47] which shows that the anionic lone pair [45, 48] with the p-state character [47] forms on $Te_{(1)}$ atoms, while lone pair Bi-s states are stereochemically inactive [45, 46].

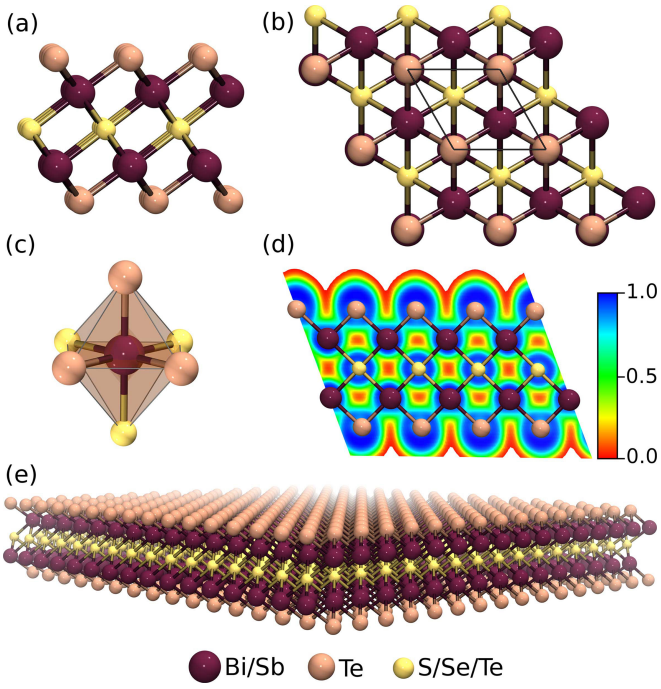

Figure 1. (a) Side and (b) top view of a quintuple layer (QL) of Bi_2Te_3 or equivalent materials. Middle layer Tellurium atom is different in its nature due to different coordination, as indicated in (c). The crystal structure consists of neighboring octahedra. (d) Electronic Localization Function (ELF) of the studied materials. Regions where the ELF is zero (one) correspond to no (full) localization. (e) Extended view of the M_2Te_2X (M=Bi, Sb; X=S, Se, Te) family of monolayers in which the middle layer is represented by yellow spheres.

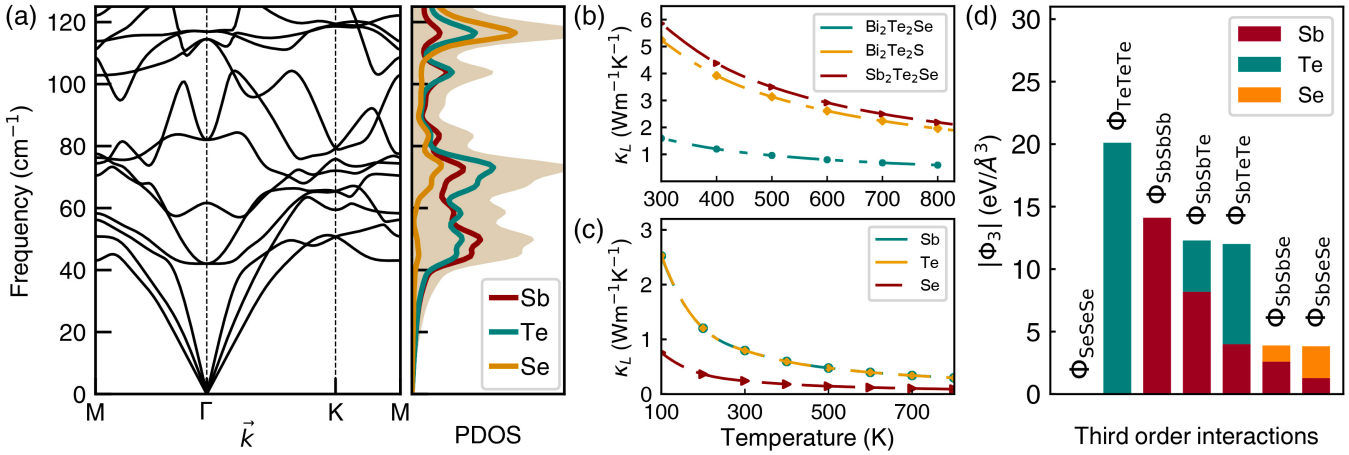

Figure 2. Phonon transport properties: (a) Phonon dispersion and the density of states (DOS) of Sb_2Te_2Se. Note the avoided crossings between optical and acoustic modes along the Γ-M and Γ-K directions. The partial DOS indicates the rather similar contributions from Sb and Te atoms to the total DOS, as well as the enhanced contribution from Se atoms in the middle layer with increased frequency. (b) Lattice thermal conductivities of the studied materials as a function of temperature from 300 to 800 K. Due to the higher average mass of Bi_2Te_2Se, its κ_L is significantly smaller than that of Sb_2Te_2Se. (c) Atom-decomposed κ_L of Sb_2Te_2Se as a function of temperature. The decomposition is according to the amplitudes of the atomic eigendisplacements, showing that Sb and Te have similar contributions to κ_L across the whole temperature range, while the contribution from Se is significantly smaller. (d) Frobenius norm of the calculated third-order inter-atomic force constants, indicating the magnitude of anharmonicity. The larger magnitude of Φ associated with Te atoms is attributed to the lone-pair electrons.

Phonon Transport Properties. Principles to find materials with intrinsically low lattice thermal conductivity, which was originally proposed by Slack [23–26], include, (i) having high average atomic mass, (ii) weak inter-atomic bonding, (iii) complex crystal structure, and (iv) strong anharmonicity, measured by Grüneisen parameter.

In many materials including monolayers, a high average mass (M_{a_v}) leads to a relatively low Debye temperature (Θ_D) and consequently low acoustic phonon velocities [24]. According to this insight, a lower lattice thermal conductivity in Bi_2Te_3 is expected compared to that of Sb_2Te_3, majorly because of the heavier atomic mass of Bi compared to Sb. On the other hand, the bond strength also plays an important role in determining the lattice thermal conductivity, *e.g.*, for monolayers of Mo and W dichalcogenides [26, 49], wherein increasing (decreasing) cation (anion) nucleon number leads to stronger (weaker) bonding and higher (lower) thermal conductivity. In this regard, the projected Crystal Orbital Overlap Population (pCOOP) and projected Crystal Orbital Hamilton Population (pCOHP) are potent tools for analyzing chemical bonds in solid [50–52]. The calculated pCOOP and pCOHP are shown in Fig. S8 of SI. The integrated values with respect to energy up to ϵ_F for both IpCOOP and IpCOHP can be used to analyze the bond strength [53, 54]: the more overlap the orbitals have, the stronger the associated bonds are. The calculated value for Sb–Te bond in Sb_2Te_2Se is about 14% higher than that of Bi–Te bond in Bi_2Te_2Se monolayers. Therefore according to Slack's theory [23], the lower thermal conductivity of Bi_2Te_2Se monolayers may be partially due to both weaker inter-atomic bonds and the heavier atomic mass of Bi compared to Sb.

Figure 2(a) shows that Sb_2Te_2Se monolayer is dynamically stable with no imaginary modes through the whole BZ. The corresponding atom-decomposed phonon density of states (DOS) shows that in frequencies ranging from 0 to just below 60 cm^{-1}—the range which contributes the most to lattice heat transport—the contribution of Sb and Te atoms to DOS are similar. The quantitative description of κ_L for the studied monolayers is shown in Figure 2(b). The κ_L of Sb_2Te_2Se is 6 Wm^{-1}K^{-1} at 300 K, much lower than the well-studied TE monolayers such as MoS_2 and WSe_2, with the κ_L of 140 and 42 Wm^{-1}K^{-1}, respectively [55]. The calculated atom-decomposed lattice thermal conductivity shows that Sb and Te atoms are equally contributing to κ_L (see Figure 2(c)), consistent with our earlier analysis of the DOS. Moreover, branch decomposed thermal conductivity (Fig. S5, SI) demonstrates that the optical branches contribute poorly to κ_L, hardly reaching 18% at high temperatures. The largest contributions belong respectively to transverse acoustic (TA), longitudinal acoustic (LA), and out-of-plane acoustic (ZA) branches. The analysis of the mean free path cumulative lattice thermal conductivity (Fig. S7, SI) reveals that the κ_L can be further suppressed by decreasing the grain size of the polycrystals; for example, at the size of 100 nm the κ_L reduces by 50%.

Grüneisen parameter (γ) measures the anharmonicity of crystalline systems and based on Slack's theory [23] it is inversely ($\kappa_L \propto \frac{1}{\gamma^2}$) related to the lattice thermal conductivity, κ_L. The larger the γ the stronger the anharmonicity and thus the lower the κ_L. The Grüneisen parameters of Sb_2Te_2Se and MoS_2 are shown in Fig. S6(d)

and for the transition metal dichalcogenides (TMDs) are reported in Ref.[56]. The calculated Grüneisen parameters of acoustic and low-lying optical modes of Sb_2Te_2Se (*i.e.*,, heat-carrying phonons) evidence not only much higher mode values than MoS_2 and other TMDs but also stronger q-dependence, rendering an intrinsic and large anharmonicity in Sb_2Te_2Se. As expected, the κ_L of Sb_2Te_2Se at 300 K ($\approx 6\,Wm^{-1}K^{-1}$) is more than 7 times lower than that of WSe_2 ($\approx 42\,Wm^{-1}K^{-1}$ [57]) while the atomic mass of W (183.84 amu) is larger than Sb (121.76 amu) and Te (127.6 amu). As discussed in the following paragraph, the origin of anharmonicity in Sb_2Te_3 is traced back to anionic lone pair of Te atoms.

To find out the fundamental origin of the anharmonicity in Sb_2Te_2Se, we calculate the norm of the third-order interatomic force constants (IFCs), which is defined as $\Phi_{mnl} = \frac{\partial^3 E}{\partial u_m \partial u_n \partial u_l}$ (E and u are the total energy and atom displacement for different atom species m, n, and l). Since (i) a large absolute value of $|\Phi|$ suggests strong anharmonicity and (i) the phonon scattering rates are roughly proportional to $|\Phi_{mnl}|^2$, it can be seen in Figure 2(d) that the strongest anharmonicity is associated with the Φ_{TeTeTe}, namely, the outer layer Te atoms where the lone pair electrons are stereochemically active. Consistent with previous studies [58, 59], the presence of lone pair electrons, localized on Te atoms, could enforce anharmonicity and subsequently lower the lattice thermal conductivity of a crystal.

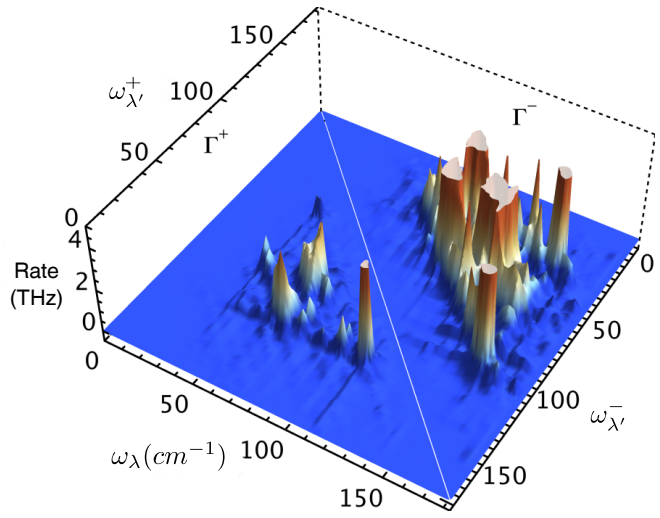

Figure 3. Contour plot of the three-phonon scattering rates associated with the absorption process (Γ^+: $\lambda + \lambda' \rightarrow \lambda''$) and the emission process (Γ^-: $\lambda \rightarrow \lambda' + \lambda''$) in Sb_2Te_2Se at 300 K. The left segment shows the absorption rates, whereas the right panel indicates the rates for emission processes. The corresponding phonon frequencies ω are given in units of cm^{-1}.

To further shed light on how phonons are scattered in Sb_2Te_2Se, we show in Figure 3 the frequency-dependent scattering rates arising from the three-phonon interactions, namely, the absorption (Γ_+: $\lambda + \lambda' \rightarrow \lambda''$) and emission ($\Gamma_-$: $\lambda \rightarrow \lambda' + \lambda''$) processes. The peaks in the scattering rates plot depict the scattering magnitude of the first phonon mode (λ) induced by the second phonon mode (λ'), satisfying both energy and crystal momentum conservation. It can be seen that the low-frequency phonon modes ($< 50\ cm^{-1}$) are only weakly scattered, which majorly originates from the absorption process, consistent with their long lifetimes as shown in Fig.S6(c). In contrast, the optical phonon modes are strongly scattered during various emission processes, resulting in small contributions to lattice heat conduction.

Electron Transport Properties. Considering the similarity in the electronic structure of the studied materials, we take Sb_2Te_2Se as an example here. As shown in Figure 4, Sb_2Te_2Se is a semiconductor with an indirect band-gap of 0.44 eV (including spin orbit coupling). Figure 4(c) (see Fig. S3, SI, for all family members) show nearly significant contributions of chalcogen and pnictide atoms in both valence and conduction bands, which is consistent with the covalent nature of bonding in this family of semiconductors [46, 47, 60]. Note that the per atom contributions from Se and Te in the calculated total DOS are similar, however, there are two times more Te atoms than Se in the unit cell, and thus a larger contribution from Te atoms in the valence band is expected.

What turns this family into outstanding and the most studied TE materials [22, 61–64], beside low lattice thermal conductivity, is their excellent electronic transport properties and relatively high PF compared to other single layer TE candidates. The feature in the band structure of these monolayers that enhances their PF is the high band degeneracy N_v, which is usually observed when several valleys with the same energies occur near the Fermi level or when the valley is located at a low symmetry point of the Brillouin zone of a high symmetry lattice (valley degeneracy). For the $R3\bar{m}$ symmetry, valley degeneracy between both Γ–M and Γ–K is 6 and thus the N_v is just six times the number of energetically degenerate valence band maximum (VBM) at different points in the Brillouin zone. The degeneracy that could occur among VBMs is indeed numerical, also called accidental [65] or band convergence [7]. Therefore, the energy differences between four potential extrema (see Fig. 4(c) for VB_1,VB_2,VB_3,VB_4) with respect to VBM is listed in Table S1, SI. As discussed in previous studies [61, 66], PF has an exponential dependent on $-\Delta E$, $PF \propto e^{-\Delta E/k_B T}$, reaching its maximum value at $\Delta E \approx 0$. As seen in Table S1 the energy difference (ΔE) between VBM (here VB_1) and the next highest VB (here VB_4) of Bi_2Te_3 and Sb_2Te_3 are 16 and 42 meV respectively, leaving one VBM at Fermi level, and leading to $N_v = 6$. Although the other three valleys are just slightly lower in energy, N_v larger than 12 is not reachable by strain engineering. That is because when strain is induced, different valleys in the band structure counteract and raising one results in lowering the others, making further tuning of the valence band insurmountable. For instance, defining $\epsilon = (a - a_0)/a$ as a measure of change in lattice constant, our calculations

for the case of Bi_2Te_3 demonstrated that only 4% strain doubled N_v from 6 to 12 and increased the PF by one-tenth (see Fig. S1, SI), but this would be an upper limit to N_v.

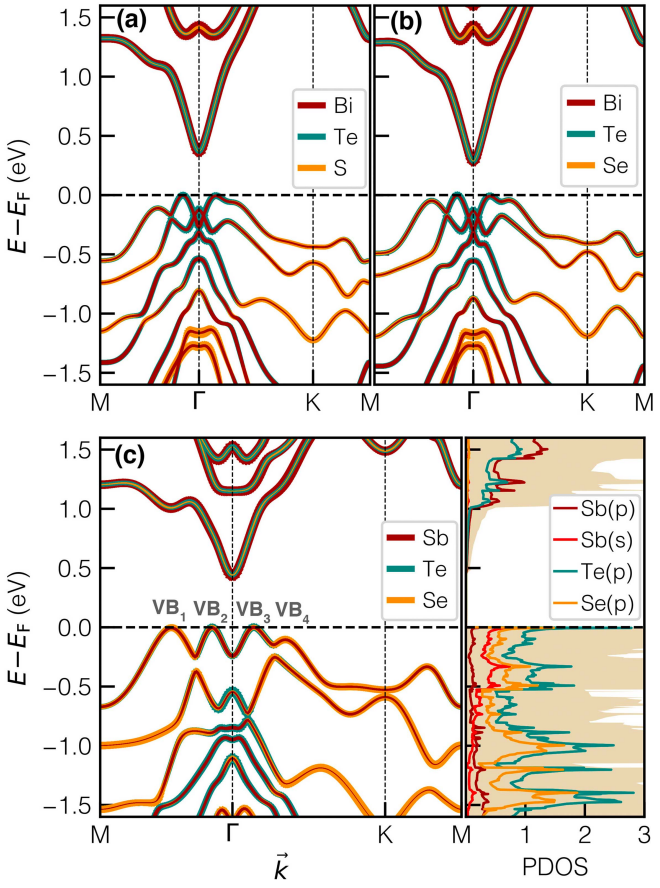

Figure 4. Atom-decomposed electronic band structures of (a) Bi_2Te_2S, (b) Bi_2Te_2Se, and (c) Sb_2Te_2Se monolayers. Considering the similar electronic properties among these three compounds, here we only plot the partial density of states (PDOS) of Sb_2Te_2Se and also remove Te(s) and Se(s) projection due to their negligible contributions (see SI for more information). The valence bands are mixed of, in order of magnitude, Te (p), Se/S (p) and Sb/Bi (s) orbitals.

Substitution of $Te_{(2)}$ atoms with S and Se adequately improves band convergence of Bi_2Te_3 and Sb_2Te_3 monolayers by lowering the ΔE to ∼4 meV which can be considered as almost degenerate extrema approaching $N_v = 12$. The giant band degeneracy of 18 occurs in Sb_2Te_2Se monolayers in which the two band extrema in Γ–M direction and the one in Γ–K direction are well-aligned (with numerical differences < 3 meV). To further understand how atom substitution leads to band alignment, we resort to atom resolved band structure calculations.

The atom decomposed band structure reveals that beside Sb/Bi atoms, the outer layer chalcogen atoms (mainly their p-state as shown in DOS of Figure 4(c)) are significantly contributing to VB_2 and VB_3: that is to say, these extrema mainly inherit the character of the $Te_{(1)}$ atoms (bold green line). On the contrary, in the VB_1 and VB_4, the middle layer chalcogen atoms (*i.e.,* $Te_{(2)}$ have the dominant contribution (bold orange line). Therefore, one can independently tune the height of $VB_{1,4}$ with respect to $VB_{2,3}$ by changing the middle layer atoms. As seen in Fig.S2, SI, substitution of the middle layer $Te_{(2)}$ atoms with the more electronegative Se ones in Sb_2Te_3 lowers the height of $VB_{1,4}$ with respect to the $VB_{2,3}$, which leads to the alignment of $VB_{1,2,3}$, and to $N_v = 18$ in Sb_2Te_2Se as highlighted in Figure 4(c). The same observation holds for S substituted monolayers, however, due to higher electronegativity of S compared to Se the VB_1 and VB_4 extrema decrease a lot that leave only the two central extrema aligned, leading to $N_v = 12$ in Sb_2Te_2S.

Using a Constant Relaxation Time Approximation (CRTA), we calculated electronic transport coefficients for Bi_2Te_2S, Bi_2Te_2Se and Sb_2Te_2Se monolayers at varying temperatures by solving the Boltzmann transport equation. To estimate electronic transport properties of materials the choice of electron relaxation time τ is critical. From comparison with experimental data at 300 K, N. F. Hinsche *et al.* [67] determined the in-plane τ=1.2×10^{-14} s and 1.1×10^{-14} s for the Sb_2Te_3 and Bi_2Te_3, respectively. Also, fitted values such as 2.2×10^{-14} s [63, 68] and $\approx 0.65 \times 10^{-14}$ [62] were suggested for Bi_2Te_3 at 300 K. Likewise, for Bi_2Te_2S the in-plane relaxation time of 3×10^{-14} s was used [69]. N. T. Hung *et al.,* [61] calculated the relaxation time τ in $Bi_2\{S, Se, Te\}_3$ monolayers and found it to be $0.2 - 0.5 \times 10^{-14}$ s, much lower than their 3D counterparts. They claimed that shorter τ for 2D materials is due to quantum confinement effect [70] which increases the density of electronic states in 2D systems. Here we use $\tau = 0.5 \times 10^{-14}$ s and 1×10^{-14} s, as suggested by Ref. [67] and Ref. [61] to estimate the zT of the studied materials. However, because of possible uncertainties in the estimation of τ and to make the comparison to previous work easier, we also report the zT and PF for different τ (color bar) within a range from 0.2 to 4.4×10^{-14} s in Fig. S9 of SI, covering all the previously reported τ.

Assuming τ=1 ×10^{-14} s, the calculated PF of Sb_2Te_2Se at three different temperatures are compared to other studied compounds. Note that the increase in PF at higher temperatures is due to a constant relaxation time adopted in all three temperatures, while in reality the relaxation time decreases with increasing temperature (roughly by $\tau \propto T^{-1.5}$ for Bi_2Te_3 [63]). As seen in Figure 5(a), using $\tau = 1 \times 10^{-14}$ s at $T = 300$ K our calculated PF for Bi_2Te_3 is about 4 mWm^{-1}K^{-2} that agrees well with the ∼ 4.4 mWm^{-1}K^{-2} reported in the previous study [63]. This PF increases to 7 mWm^{-1}K^{-2} by substitution of Te with Se atom as in Bi_2Te_2Se. Likewise, the PF of Sb_2Te_3 increases by a factor of two upon Se substitution, achieving a giant PF=10 mWm^{-1}K^{-2} in Sb_2Te_2Se at 300 K as seen in Figure 5(b). Using the same τ and temperature, the maximum PF for MoS_2, $MoSe_2$, TiS_3, Pd_2Se_3 are respectively 1.8 mWm^{-1}K^{-2} [71] (n-type),

0.8 $mWm^{-1}K^{-2}$ [55] (n-type) and 1.8 $mWm^{-1}K^{-2}$ [72] (n-type) and 1.6 $mWm^{-1}K^{-2}$ [25] (p-type). Due to the much larger PF and much smaller κ_L compared to these materials (*e.g.*, κ_L of Sb_2Te_2Se at 300 K is 6 $Wm^{-1}K^{-1}$ and MoS_2 131 $Wm^{-1}K^{-1}$ [57]) we expect a high figure of merit in Sb_2Te_2Se, thus enabling high thermoelectric efficiency.

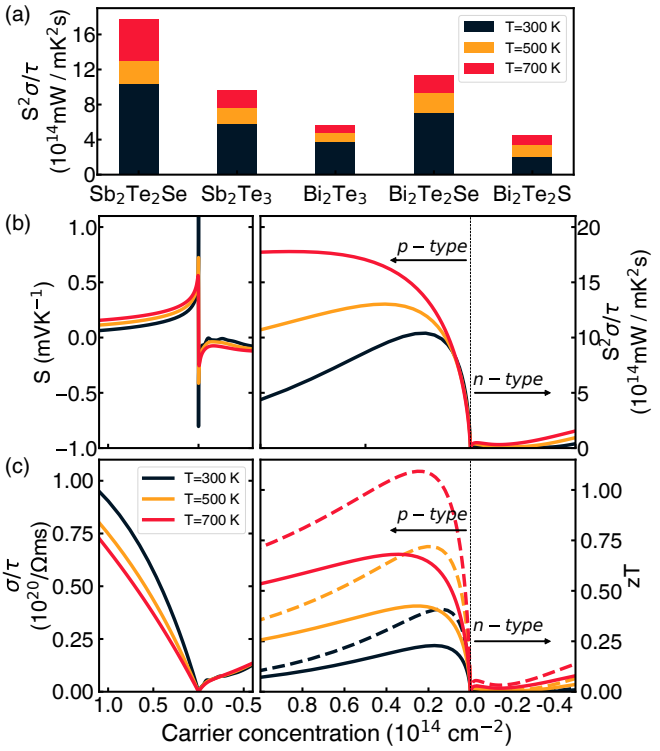

Figure 5. (a) Optimal PF of different monolayer compounds are presented at 300, 500 and 700 K for the purpose of comparison. The figure indicates a PF increase in newly proposed materials, Sb_2Te_2Se and Bi_2Te_2Se, with respect to their parents. (b) Transport coefficients (PF, S), and (c) σ and zT of Sb_2Te_2Se as a function of carrier concentrations as functions of temperatures and relaxation times. Solid and dashed lines represent zT values associated with τ=0.5 and 1.0 $\times 10^{-14}$ s, respectively.

Thermoelectric Figure of Merit. Figure 5(c) shows the calculated zT for the Sb_2Te_2Se at three different relaxation times and temperatures. Even assuming τ as small as 0.5×10^{-14} s we could reach the zT of 0.7 and 0.22 at 700 and 300 K, respectively. Considering the same relaxation time, the calculated zT values are much larger than other proposed monolayers such as WSe_2 [55] and TiS_3 [72] and SnSe [73]. For example, using the same τ the calculated zT= 0.7 at 700 K for Sb_2Te_2Se is 30% larger than SnSe monolayers [73], which has the highest record zT in the bulk phase [74].

It is worth nothing that the estimated zT in this work could be considered as a lower limit, because the used electron relaxation time is quite small and the calculated κ_L tends to be larger than the experimental one. For example, the calculated κ_L for MoS_2 monolayers is 131 $Wm^{-1}K^{-1}$ [57] while experimental value of 34.5 $Wm^{-1}K^{-1}$ was measured [75], which could be due to point defects, dislocations, and finite size effect. Therefore, the real zT could be larger than our estimation.

Conclusions

We investigated electronic structure, phonon and electron transport properties of M_2Te_2X (M=Bi, Sb; X=S, Se, Te) monolayers by the means of first-principles calculations and Boltzmann transport theory. Our detailed analysis reveal that four reachable valence band extrema exist in this family of materials and that two of them merely depends on the electronegativity of the middle layer chalcogen atoms, which makes the independent modulation of the vallyes' position doable. As such we substitute the middle layer Te with isoelectronic equivalents S, and Se atoms and found that the band alignment significantly improves transport properties of both Bi_2Te_3 and Sb_2Te_3. The superior valence band alignment occurs in Sb_2Te_2Se monolayers where the trhee out of four possible valleys are well-aligned resulting in the giant band degeneracy of 18 that the hold a record among all thermoelectric materials. Our results demonstrate that zT in this family of monolayers, is comparable to, and can be better than many well-known thermoelectric compounds. It should also be noted that the reported values for zT in these materials are only lower limits, since nanostructuring can significantly deteriorate lattice thermal conductivity by almost 50 percent. Our finding could advance the thermoelectric materials design, where the convergence of electronic band is achieved by tuning the composition.

[1] H. J. Goldsmid, *Introduction to thermoelectricity*, Vol. 121 (Springer, 2010).
[2] J. Tang, H.-T. Wang, D. H. Lee, M. Fardy, Z. Huo, T. P. Russell, and P. Yang, Nano letters **10**, 4279 (2010).
[3] A. Majumdar, Science **303**, 777 (2004).
[4] B. Poudel, Q. Hao, Y. Ma, Y. Lan, A. Minnich, B. Yu, X. Yan, D. Wang, A. Muto, D. Vashaee, *et al.*, Science **320**, 634 (2008).
[5] M. Dresselhaus, G. Dresselhaus, X. Sun, Z. Zhang, S. Cronin, and T. Koga, Physics of the Solid State **41**, 679 (1999).
[6] W. Liu, X. Tan, K. Yin, H. Liu, X. Tang, J. Shi, Q. Zhang, and C. Uher, Physical Review Letters **108**, 166601 (2012).
[7] Y. Tang, Z. M. Gibbs, L. A. Agapito, G. Li, H.-S. Kim, M. B. Nardelli, S. Curtarolo, and G. J. Snyder, Nature materials **14**, 1223 (2015).
[8] Q. Zhang, F. Cao, W. Liu, K. Lukas, B. Yu, S. Chen, C. Opeil, D. Broido, G. Chen, and Z. Ren, Journal of the American chemical society **134**, 10031 (2012).
[9] E. Witkoske, X. Wang, M. Lundstrom, V. Askarpour, and J. Maassen, Journal of Applied Physics **122**, 175102 (2017).
[10] Y. Pei, X. Shi, A. LaLonde, H. Wang, L. Chen, and G. J. Snyder, Nature **473**, 66 (2011).
[11] Y. Pei, H. Wang, and G. J. Snyder, Advanced materials **24**, 6125 (2012).
[12] J. He, S. Hao, Y. Xia, S. S. Naghavi, V. Ozolins, and C. Wolverton, Chemistry of Materials **29**, 2529 (2017).
[13] J. He, Y. Xia, S. S. Naghavi, V. Ozoliņš, and C. Wolverton, Nature communications **10**, 719 (2019).
[14] H. Goldsmid, *Thermoelectric refrigeration* (Springer, 2013).
[15] D. Wright, Nature **181**, 834 (1958).
[16] H.-S. Kim, N. A. Heinz, Z. M. Gibbs, Y. Tang, S. D. Kang, and G. J. Snyder, Materials Today **20**, 452 (2017).
[17] X. Yan, B. Poudel, Y. Ma, W. Liu, G. Joshi, H. Wang, Y. Lan, D. Wang, G. Chen, and Z. Ren, Nano letters **10**, 3373 (2010).
[18] H. Shi, D. Parker, M.-H. Du, and D. J. Singh, Physical Review Applied **3**, 014004 (2015).
[19] H. Goldsmid, Proceedings of the Physical Society. Section B **69**, 203 (1956).
[20] T. M. Tritt and M. Subramanian, MRS bulletin **31**, 188 (2006).
[21] G. Zhang, B. Kirk, L. A. Jauregui, H. Yang, X. Xu, Y. P. Chen, and Y. Wu, Nano letters **12**, 56 (2011).
[22] S. Sharma and U. Schwingenschlögl, ACS Energy Lett. **1**, 875 (2016).
[23] G. A. Slack, Journal of Physics and Chemistry of Solids **34**, 321 (1973).
[24] L. Lindsay, D. Broido, and T. Reinecke, Physical review letters **111**, 025901 (2013).
[25] S. S. Naghavi, J. He, Y. Xia, and C. Wolverton, Chemistry of Materials **30**, 5639 (2018).
[26] B. Peng, H. Zhang, H. Shao, Y. Xu, R. Zhang, H. Lu, D. W. Zhang, and H. Zhu, ACS applied materials & interfaces **8**, 20977 (2016).
[27] G. Ceder and K. Persson, "The materials project: A materials genome approach," (2010).
[28] S. P. Ong, L. Wang, B. Kang, and G. Ceder, Chemistry of Materials **20**, 1798 (2008).
[29] A. Jain, G. Hautier, S. P. Ong, C. J. Moore, C. C. Fischer, K. A. Persson, and G. Ceder, Physical Review B **84**, 045115 (2011).
[30] N. Mounet, M. Gibertini, P. Schwaller, D. Campi, A. Merkys, A. Marrazzo, T. Sohier, I. E. Castelli, A. Cepellotti, G. Pizzi, *et al.*, Nature nanotechnology **13**, 246 (2018).
[31] M. Kanagaraj, A. Pawbake, S. C. Sarma, V. Rajaji, C. Narayana, M.-A. Measson, and S. C. Peter, Journal of Alloys and Compounds **794**, 195 (2019).
[32] G. Kresse and J. Hafner, Physical Review B **48**, 13115 (1993).
[33] G. Kresse and J. Furthmüller, Computational materials science **6**, 15 (1996).
[34] P. E. Blöchl, Physical review B **50**, 17953 (1994).
[35] G. Kresse and D. Joubert, Physical review b **59**, 1758 (1999).
[36] J. P. Perdew, K. Burke, and M. Ernzerhof, Physical review letters **77**, 3865 (1996).
[37] G. K. Madsen and D. J. Singh, Computer Physics Communications **175**, 67 (2006).
[38] A. Togo, F. Oba, and I. Tanaka, Physical Review B **78**, 134106 (2008).
[39] W. Li, J. Carrete, N. A. Katcho, and N. Mingo, Computer Physics Communications **185**, 1747 (2014).
[40] X. Luo, M. B. Sullivan, and S. Y. Quek, Physical Review B **86**, 184111 (2012).
[41] T. Björkman, A. Gulans, A. V. Krasheninnikov, and R. M. Nieminen, Physical review letters **108**, 235502 (2012).
[42] A. Ambrosi and M. Pumera, Chemical Society Reviews **47**, 7213 (2018).
[43] D. L. Greenaway and G. Harbeke, Journal of Physics and Chemistry of Solids **26**, 1585 (1965).
[44] A. D. Becke and K. E. Edgecombe, The Journal of chemical physics **92**, 5397 (1990).
[45] A. Walsh, D. J. Payne, R. G. Egdell, and G. W. Watson, Chemical Society Reviews **40**, 4455 (2011).
[46] I. T. Witting, T. C. Chasapis, F. Ricci, M. Peters, N. A. Heinz, G. Hautier, and G. J. Snyder, Advanced Electronic Materials , 1800904 (2019).
[47] T. H. Lee and S. R. Elliott, Advanced Materials **29**, 1700814 (2017).
[48] J. L. Da Silva, A. Walsh, and H. Lee, Physical Review B **78**, 224111 (2008).
[49] L.-F. Huang and Z. Zeng, The Journal of Physical Chemistry C **119**, 18779 (2015).
[50] V. L. Deringer, A. L. Tchougreeff, and R. Dronskowski, J. Phys. Chem. A **115**, 5461 (2011).
[51] R. Dronskowski and P. E. Bloechl, J. Phys. Chem. **97**, 8617 (1993).
[52] R. Hoffmann, Angew. Chem. Int. Ed. Engl. **26**, 846 (1987).
[53] S. Maintz, V. L. Deringer, A. L. Tchougréeff, and R. Dronskowski, Journal of computational chemistry **37**, 1030 (2016).
[54] S. Maintz, V. L. Deringer, A. L. Tchougréeff, and R. Dronskowski, Journal of computational chemistry **34**, 2557 (2013).
[55] S. Kumar and U. Schwingenschlogl, Chemistry of Materials **27**, 1278 (2015).
[56] B. Peng, H. Zhang, H. Shao, Y. Xu, X. Zhang, and H. Zhu, RSC Adv. **6**, 5767 (2016).

[57] A. N. Gandi and U. Schwingenschlögl, EPL (Europhysics Lett. **113**, 36002 (2016).
[58] M. Dutta, K. Pal, U. V. Waghmare, and K. Biswas, Chemical science **10**, 4905 (2019).
[59] M. D. Nielsen, V. Ozolins, and J. P. Heremans, Energy & Environmental Science **6**, 570 (2013).
[60] V. L. Deringer, R. P. Stoffel, M. Wuttig, and R. Dronskowski, Chemical Science **6**, 5255 (2015).
[61] N. T. Hung, A. R. Nugraha, and R. Saito, Nano Energy **58**, 743 (2019).
[62] C. Lee, J. N. Kim, J.-Y. Tak, H. K. Cho, J. H. Shim, Y. S. Lim, and M.-H. Whangbo, AIP Adv. **8**, 115213 (2018).
[63] G. Zhou and D. Wang, Sci. Rep. **5** (2015).
[64] B. Xu, J. Zhang, G. Yu, S. Ma, Y. Wang, and Y. Wang, J. Appl. Phys. **124**, 165104 (2018).
[65] K. F. Garrity, Physical Review B **94**, 045122 (2016).
[66] N. T. Hung, A. R. Nugraha, T. Yang, Z. Zhang, and R. Saito, Journal of Applied Physics **125**, 082502 (2019).
[67] N. Hinsche, B. Y. Yavorsky, I. Mertig, and P. Zahn, Physical Review B **84**, 165214 (2011).
[68] T. J. Scheidemantel, C. Ambrosch-Draxl, T. Thonhauser, J. V. Badding, and J. O. Sofo, Phys. Rev. B **68**, 125210 (2003).
[69] S.-J. Joo, B. Ryu, J.-H. Son, J. E. Lee, B.-K. Min, and B.-S. Kim, Journal of Alloys and Compounds **783**, 448 (2019).
[70] L. Hicks and M. S. Dresselhaus, Physical Review B **47**, 12727 (1993).
[71] H. Babaei, J. Khodadadi, and S. Sinha, Applied Physics Letters **105**, 193901 (2014).
[72] J. Zhang, X. Liu, Y. Wen, L. Shi, R. Chen, H. Liu, and B. Shan, ACS Appl. Mater. Interfaces **9**, 2509 (2017).
[73] F. Q. Wang, S. Zhang, J. Yu, and Q. Wang, Nanoscale **7**, 15962 (2015).
[74] L.-D. Zhao, S.-H. Lo, Y. Zhang, H. Sun, G. Tan, C. Uher, C. Wolverton, V. P. Dravid, and M. G. Kanatzidis, Nature **508**, 373 (2014).
[75] R. Yan, J. R. Simpson, S. Bertolazzi, J. Brivio, M. Watson, X. Wu, A. Kis, T. Luo, A. R. Hight Walker, and H. G. Xing, ACS Nano **8**, 986 (2014).